



HAL
open science

Influence of the Initial Beach Profile on the Sediment Transport Processes During Post-Storm Onshore Bar Migration

Florian Grossmann, David Hurther, Agustín Sánchez-Arcilla, José M. Alsina

► **To cite this version:**

Florian Grossmann, David Hurther, Agustín Sánchez-Arcilla, José M. Alsina. Influence of the Initial Beach Profile on the Sediment Transport Processes During Post-Storm Onshore Bar Migration. *Journal of Geophysical Research. Oceans*, 2023, 128 (4), 10.1029/2022JC019299 . hal-04259913

HAL Id: hal-04259913



<https://hal.science/hal-04259913v1>

Submitted on 26 Oct 2023

HAL is a multi-disciplinary open access archive for the deposit and dissemination of scientific research documents, whether they are published or not. The documents may come from teaching and research institutions in France or abroad, or from public or private research centers.

L'archive ouverte pluridisciplinaire **HAL**, est destinée au dépôt et à la diffusion de documents scientifiques de niveau recherche, publiés ou non, émanant des établissements d'enseignement et de recherche français ou étrangers, des laboratoires publics ou privés.

Influence of the Initial Beach Profile on the Sediment Transport Processes During Post-Storm Onshore Bar Migration

Florian Grossmann^{1,2} , David Hurther³, Agustín Sánchez-Arcilla¹ , and José M. Alsina¹ 

¹Universitat Politècnica de Catalunya, Barcelona, Spain, ²Department of Civil and Environmental Engineering, Laboratory of Maritime Engineering, Universitat Politècnica de Catalunya, Barcelona, Spain, ³Laboratory of Geophysical and Industrial Flows (LEGI), CNRS, Grenoble INP, Université Grenoble Alpes, Grenoble, France

Key Points:

- Accretive wave condition determines quasi-equilibrium recovery beach profile irrespective of initial profiles
- Configuration of post-storm profiles determines type of accretive morphological evolution toward the quasi-equilibrium profile
- Outer bar maintenance associated with wave breaking over the bar while breaking farther onshore leads to outer bar dissipation

Supporting Information:

Supporting Information may be found in the online version of this article.

Correspondence to:

F. Grossmann,
florian.grossmann@upc.edu

Citation:

Grossmann, F., Hurther, D., Sánchez-Arcilla, A., & Alsina, J. M. (2023). Influence of the initial beach profile on the sediment transport processes during post-storm onshore bar migration. *Journal of Geophysical Research: Oceans*, 128, e2022JC019299. <https://doi.org/10.1029/2022JC019299>

Received 16 SEP 2022
Accepted 21 MAR 2023

Abstract Onshore bar migration is a characteristic bar behavior during post-storm beach recovery. The present large-scale experiments, feature bichromatic wave groups over an initially steep (1:15), fully-evolving beach. The same accretive wave condition is applied on two different post-storm beach profiles featuring outer and inner bars. They are characterized by a larger (smaller) shoreline erosion and a larger (smaller) outer breaker bar located farther away from (closer to) the shoreline depending on the larger (smaller) energy of the storm condition. After a considerable post-storm recovery time, similar equilibrium profiles are obtained, stressing the link between wave condition and equilibrium beach configuration. However, the evolution toward the equilibrium is different and depends on the initial morphological condition (post-storm beach profile). After the larger storm, the morphological evolution is termed accretive merging (AM) and characterized by merging of the two bars (outer bar dissipation). After the smaller storm, the morphological evolution denoted as accretive non-merging (AN) is characterized by onshore migration of the two bars with constant distance between them (bar maintenance). This study focuses on processes around the outer bar. During AN it features wave breaking, causing large suspended net offshore transport. AM, in contrast, mainly features bedload related to short wave asymmetries and low decomposed net transport rate magnitudes. High suspended net offshore transport occurs solely onshore of the outer bar trough. This causes filling of the bar trough and bar dissipation during migration. Additionally, processes around the outer bars are linked to accretion onshore of the bars and at the shoreline.

Plain Language Summary Nearshore sandbars are seabed features that protect coastal infrastructure behind many sandy beaches around the world. In response to waves they change in shape and distance to the beach, playing a key role in beach recovery after storms. To improve understanding of their onshore movement (migration), experiments were conducted which represented natural conditions in a controlled laboratory setting. In this context, the underwater transport of sand was measured. Application of the same recovery wave condition to two different post-storm beach profiles resulted in two different types of bar onshore migration. After long experimental duration, both types evolved toward relatively similar beach profiles but the different ways of reaching them might have important practical consequences. In general, bar migration was governed by the interaction of onshore- and offshore-transporting processes. They, in turn, were influenced by wave breaking. Bars, furthermore, cause wave breaking—closing the feedback loop. Ultimately, the different wave breaking locations, resulting from the shape of the post-storm profiles, caused the different types of bar onshore migration during recovery. The present results provide crucial information for the development of mathematical models to forecast beach evolution and safeguard human interests in the coastal zone.

1. Introduction

Storms (erosive wave conditions) on sandy coasts reshape the beach profile and threaten human interests in the coastal zone. They are often followed by beach recovery (accretive wave conditions) which slowly reverses the storms' morphological changes (e.g., Gallagher et al., 1998; Wright & Short, 1984). During storms, bar offshore migration characterizes morphological evolution and the shoreline erodes. Beach recovery, on the other hand, features bar onshore migration and the shoreline accretes. Note that bars play important roles in wave energy dissipation and coastal management, especially in the context of storms. During beach recovery, however, their role for morphological evolution of the entire beach profile and their migration mechanisms are less clear.

© 2023. The Authors.

This is an open access article under the terms of the [Creative Commons Attribution-NonCommercial-NoDerivs License](https://creativecommons.org/licenses/by-nc-nd/4.0/), which permits use and distribution in any medium, provided the original work is properly cited, the use is non-commercial and no modifications or adaptations are made.

Certain field experiments (e.g., Phillips et al., 2017; Ruiz de Alegría-Arzaburu & Vidal-Ruiz, 2018) highlight a tendency of onshore-migrating bars to merge with the shoreline (dissipate) while others (e.g., Cheng & Wang, 2018; Gallagher et al., 1998; Kuriyama, 2002; Trowbridge & Young, 1989) observe onshore migration at near-constant form (either one or two bars). Unfortunately, it is difficult to obtain detailed data (e.g., bedload sediment transport) in such field experiments and hydrodynamic conditions often change during the long time periods required for recovery. Therefore, most studies are only based on beach profile measurements at low temporal resolution and the details of sediment transport processes and morphological evolution (such as transitions between different types of evolution) may have been missed. Certain laboratory experiments (e.g., Baldock et al., 2017; Eichentopf et al., 2018; Eichentopf, van der Zanden, et al., 2020) also observe onshore-migrating bar dissipation while others (e.g., Baldock et al., 2011; Eichentopf et al., 2018; Yoon & Cox, 2010) observe onshore migration at near-constant form. Even though some experiments featured a much higher level of detail than common in the field (e.g., Mieras et al., 2019), to the authors' knowledge no experiment has combined detailed sediment transport measurements with fully-evolving, large-scale accretive beach profiles. Thus, it is not surprising that there is a knowledge gap regarding the morphological evolution and transport processes of onshore-migrating bars.

This is highlighted by the difficulty in replicating bar onshore migration and long-term morphological evolution with process-based numerical models (e.g., van Rijn et al., 2011). The difficulties originate from complex sediment transport processes which cannot be fully resolved or are not fully understood, requiring specific model calibration (e.g., Dubarbier et al., 2015) and addition of external, calibrated onshore transport (e.g., Hoefel & Elgar, 2003; Rafati et al., 2021). To sidestep such difficulties, equilibrium-type models focus (while only considering transport processes implicitly) on quasi-equilibrium states between instantaneous hydrodynamics and instantaneous beach profile shape—either in terms of energy or dimensionless fall velocity disequilibria (e.g., Birrien et al., 2018; Davidson et al., 2013; Dean, 1977; Yates et al., 2009). Here, “quasi-equilibrium” refers to the fact that many analyses assume equilibrium to have been reached once beach profile changes are negligibly low (e.g., Baldock et al., 2017; Eichentopf, van der Zanden, et al., 2020).

In this context, the initial beach profile after a change of wave conditions plays an important role because it determines the disequilibrium that drives morphological evolution and should, in general, decrease the longer a wave condition is continuously applied. Interestingly, continued bar offshore migration (e.g., Sánchez-Arcilla et al., 1994) and shoreline erosion (e.g., Baldock et al., 2017; Sánchez-Arcilla et al., 2011) were observed even after a change from erosive to accretive conditions. This has been linked to hysteresis effects, which may have important consequences for equilibrium-type models (e.g., Birrien et al., 2018) and practical engineering purposes (e.g., coastal management strategies).

Equilibrium-type models often assume morphological evolution toward equilibrium without detailed consideration of the processes leading to such behavior because the complex links between morphology, hydrodynamics and sediment transport are often not understood in detail. Therefore, this paper investigates (a) the hydrodynamic and sediment transport processes behind onshore bar migration (beach recovery) and (b) the role of initial (post-storm) morphology in accretive morphological evolution. In the present large-scale experiments, application of the same wave condition, starting from two different beach profiles, resulted in two different types of morphological evolution toward relatively similar quasi-equilibrium beach profiles. State of the art measurements (Hurther et al., 2011) of sediment transport with particularly high resolution near the bed, including bedload transport, provide details on the related transport processes leading to the two types of morphological evolution. The introduction is followed (Section 2) by a summary of the experimental setup (reported in detail in Grossmann et al. (2022)) and the results (Section 3). Discussion of the results (Section 4) is followed by the conclusions (Section 5).

2. Experimental Setup and Data Analysis

The present data were acquired within the HYDRALAB + transnational access project “Influence of storm sequencing and beach recovery on sediment transport and beach resilience” (RESIST). Details of the experimental protocol and data analysis were already presented in Eichentopf, van der Zanden, et al. (2020) and Grossmann et al. (2022). Therefore, only the most important aspects will be repeated here.

2.1. Facility and Test Conditions

The experiments were conducted in the large-scale CIEM wave flume at the Universitat Politècnica de Catalunya (UPC) in Barcelona. The flume is 100 m long, 3 m wide and 4.5 m deep, and is equipped with a

Table 1
Wave Sequences in RESIST

Sequence	Test number	Wave condition	Duration (min)	Ω (-)	Morphology
1	16	B	30	2.21	-
	17–23	E1	240	3.34	-
	24–31	A1	360	1.44	AM
	32–35	A1	240	1.44	AN
	36–39	E2	120	2.54	-
2	40–51	A1	600	1.44	AN
	52	B	30	2.21	-
	53–56	E2	120	2.54	-
	57–68	A1	600	1.44	AN
	69–74	E1	240	3.34	-
3	75–82	A1	360	1.44	AM
	83–86	A1	240	1.44	AN
	87	B	30	2.21	-
	88–91	E1	240	3.34	-
	92–104	A2	780	1.05	-
105–108	E2	120	2.54	-	
109–132	A3	1,440	0.72	-	

Note. A1 (accretive) sequences differentiated on the basis of their morphological evolution: Accretive Merging (AM, light blue) and Accretive Non-Merging (AN, light red). Benchmark (B) random waves homogenized and compacted the manually shaped profile before start of the actual experiments.

wedge-type wave paddle. The cross-shore coordinate x was defined as 0 at the wave paddle, increasing toward the beach. The absolute vertical coordinate z refers to the still water level (SWL) while the bed-referenced coordinates ζ and ζ' refer to the seabed and point upwards. ζ accounts for continuous bed evolution throughout the tests, establishing the same vertical reference system for all ensembles measured during a test (being the bed elevation during the first velocity upcrossing of each ensemble). ζ' additionally references each measurement to the instantaneous bed elevation at which it was measured, ensuring that time-averaging and frequency filtering do not consider values below this elevation. The difference between ζ and ζ' is that the ζ bed level oscillates between positive and negative values with respect to a reference level set for each realization whereas ζ' displays only positive bed elevation values with respect to the instantaneous bed elevation. For more details on the vertical reference systems see Grossmann et al. (2022). The flume contained medium-grained sand with a median sediment diameter (D_{50}) of 0.25 mm and a measured still water settling velocity w_s of 0.034 m/s.

Bichromatic (to facilitate frequency separation) erosive (E1 and E2) and accretive (A1, A2, and A3) waves were applied in three different sequences (Table 1). They are termed erosive and accretive because of their different dimensionless sediment fall velocities ($\Omega_{rms} = \frac{H_{rms}}{T_p * w_s}$). All four A1 testing sequences with onshore-migrating bars started from a well-developed outer breaker bar formed during previous high energy tests with E1 or E2. Analysis of profile evolution over the storm sequences (Eichentopf, van der Zanden, et al., 2020) showed that under A1 the same quasi-equilibrium profiles were reached, irrespective of the initial post-storm profiles (E1 or E2). Subsequently, details on hydrodynamics, morphological evolution and sediment transport under E2 were added in Grossmann et al. (2022). This showed that the dominance of current-related suspended net offshore transport over short wave-related bedload net onshore transport caused the bar offshore migration.

Comparison to certain A1 tests (Grossmann et al., 2023) explained the change of bar migration direction under accretive waves. It was caused by decreased sediment entrainment, mixing, and undertow magnitude while asymmetry-related onshore transport stayed relatively high under A1. The present publication compares A1 tests starting from different initial profiles (after E1 and E2), investigating the resulting differences in sediment transport processes and how they led to different types of bar onshore migration toward relatively similar quasi-equilibrium profiles.

Primary frequency components in A1 were $f_1 = 0.2276$ Hz and $f_2 = 0.1979$ Hz (for similar details on the erosive wave conditions see Table S1 in Supporting Information S1). Their wave group period (T_g) is defined as $T_g = \frac{1}{f_1 - f_2} = 33.67$ s and there were seven short waves per group. The waves were characterized by a primary mean period of $T_p = \frac{1}{f_p} = 4.7$ s where $f_p = \frac{f_1 + f_2}{2}$. The repetition period (T_r), that is, the period after which a wave phase repeated exactly, contained three slightly differing, alternating wave groups so that $T_r = 3 \cdot T_g = 101.01$ s. In this study, T_r was of central importance because it determined the exact repetition for the ensemble-averaging procedure.

2.2. Instrumentation

The primary measurements were taken from a mobile frame which was re-positioned horizontally at intervals to measure in various locations surrounding the outer breaker bar. The Acoustic Concentration and Velocity Profiler (ACVP; Hurther et al., 2011) measured sediment concentrations, velocities and instantaneous bed elevations below the mobile frame. The co-located sediment concentration and velocity measurements (cross-shore and vertical) were provided as vertical profiles (1.5 mm bin size) of up to 20 cm above the seabed. Additional concentration measurements inside the ACVP measuring domain were obtained from a three-nozzle Transverse Suction

System (TSS) on the mobile frame (used for measurement validation as described in Grossmann et al. (2022)). Above the ACVP measuring domain, two Optical Backscatter Sensors (OBSs) were used to measure sediment concentrations at 40 Hz. Pointwise three-component outer flow velocities (i.e., higher than 10 cm from the bed) were measured at 100 Hz using a vertical array of three Nortek Vectrino Acoustic Doppler Velocimeters (ADV). The lowermost ADV was located within the ACVP measuring domain, approximately 10–15 cm above the seabed. The other two mobile frame ADVs were located approximately 20–25 and 30–35 cm above the seabed respectively. Water surface elevations were measured at 40 Hz using Resistive (wire) Wave Gauges (RWGs), Acoustic Wave Gauges (AWGs) and Pressure Transducers (PTs; conversion from pressure to water surface elevation following Bonneton et al. (2018)) in fixed locations along the flume. Additionally, one PT was attached to the mobile frame. Active beach profile transects were measured in intervals of 30 (60) min (depending on morphological evolution rate) with a mechanical profiler. The measurements were conducted along the centerline of the flume with a cross-shore resolution of 0.02 m and a vertical measuring accuracy of 0.01 m.

2.3. Data Treatment

The same data cleaning and averaging procedures as explained in Grossmann et al. (2022) were applied. Net sediment transport rates were calculated from beach profile transect measurements using the Exner equation (e.g., Baldock et al., 2011). The ACVP supplies profiles of acoustic backscatter intensity and sediment concentration information can be derived following the methodology of Hurther et al. (2011). This is done by iterating downwards from the emitter while accounting for the signal attenuation due to sand grain scattering and water absorption occurring along the acoustic path, as described in detail by Fromant et al. (2018). This requires a single calibration constant which was equal in all the present tests. Its value was adjusted to obtain the best fit of the ACVP measurements with TSS time-averaged concentration measurements and net transport rates from the Exner equation in all the present tests.

Sediment fluxes, q , from ACVP and OBS/ADV were calculated and decomposed into suspended load and bedload as well as short wave-, infragravity wave-, and current-related transport (for details refer to Grossmann et al. (2022)). For total net transport rates, Q , depth-integrals were calculated at every measuring instant of T_i over the total vertical domain available from ACVP, OBS and ADV. For bedload net transport rates, instantaneous bed levels and upper sheet flow limits (based on the 8%-volumetric criterion; Dohmen-Janssen et al., 2001) were used as integration boundaries (both boundaries within the ACVP measuring domain). For suspended load net transport rates, upper sheet flow limits and the upper ends of the domain available from ACVP, OBS, and ADV were used as integration boundaries.

Data from multiple tests under the same wave condition were aggregated to provide a cross-shore resolution of detailed measurements around the onshore- and offshore-migrating bars. This was done by normalizing the cross-shore location of measurements from the mobile frame with the location of visually-identified outer bar crests (as explained in Grossmann et al. (2022)). The outer bar was chosen as the reference point because it is subject to large changes during morphological evolution and characterizes the beach state (e.g., Wright & Short, 1984). The normalization is based on the assumption that in all considered tests of a certain wave condition the same type of morphological evolution (described in the following section) occurs. This was confirmed by careful profile evolution analysis (not shown for brevity; see also Grossmann et al. (2022)). The analysis showed that relative rather than absolute cross-shore coordinates determined bed evolution, profiles in the considered tests had a very similar shape in the vicinity of the outer bar crest (3.5 m offshore and onshore of it) and bars had similar heights and similar freeboard.

3. Results

3.1. Morphological Evolution

Before the application of accretive wave condition A1, the erosive wave conditions E1 and E2 (Table 1) led to the formation of a larger, outer breaker bar and a smaller, inner breaker bar. In this context, E1 represented a more energetic wave condition than E2, thus producing a quasi-equilibrium outer breaker bar farther offshore and with larger freeboard than E2.

Application of accretive wave condition A1 on E1 quasi-equilibrium profiles leads to the accretive merging (AM) morphological evolution exemplified in Figure 1a. It is characterized by rapid onshore migration and slight dissipation of the outer bar ($61 < x < 67.5$ m) while the inner bar stays in the same position ($67.5 < x < 71$ m). At the same time, the inner bar's shape gets more accentuated, there is accretion onshore of the bars ($74 < x < 77$ m) and a berm is built at the beach ($x > 77$ m). When the bars merge (Figure 1a, test 82), the inner bar becomes the new

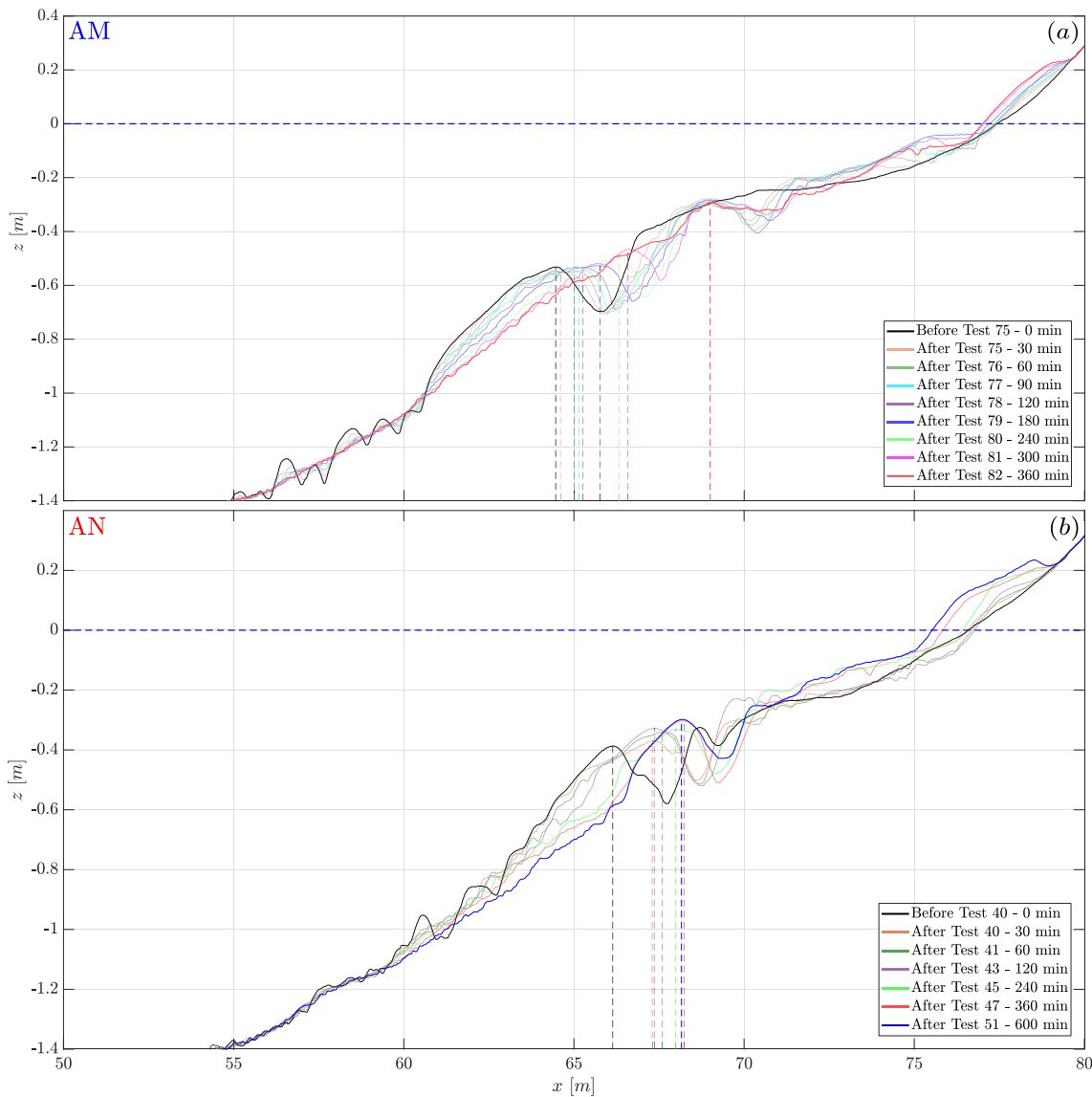


Figure 1. Examples of accretive profile evolution with merging (a) and non-merging (b) outer bars in RESIST. Still water level in dark blue dashed and profiles in various colors (solid lines). Bar maxima as dashed vertical lines.

outer bar (see vertical dashed lines in the figure) and can be considered the “active” bar (e.g., Birrien et al., 2018) with waves breaking on top of its crest.

Application of accretive wave condition A1 on E2 (less energetic than E1) quasi-equilibrium profiles leads to the accretive non-merging (AN) morphological evolution exemplified in Figure 1b, and analyzed in detail by Grossmann et al. (2023). Here, both the outer ($61 < x < 68.5$ m) and the inner ($68.5 < x < 71$ m) bar migrate onshore while keeping a constant distance between them. The bars do not merge and the outer bar appears to be the “active” one throughout morphological evolution. The accretion onshore of the bars and the berm construction at the beach, which was observed for AM, seem even more effective during AN (especially after more than 120 min of testing). The outer bar onshore migration is much slower but, in contrast to AM, it does not dissipate during evolution toward quasi-equilibrium.

Similar characteristics of morphological evolution (constant distance between the bars, active outer bar, substantial accretion onshore of bars and berm construction) become visible after the bars have merged (Figure 2a). Therefore, the merging marks a transition from AM to AN and the 240 min of A1 testing after bar merging are considered AN (see Table 1). Furthermore, after merging the new outer bar gets more accentuated and moves

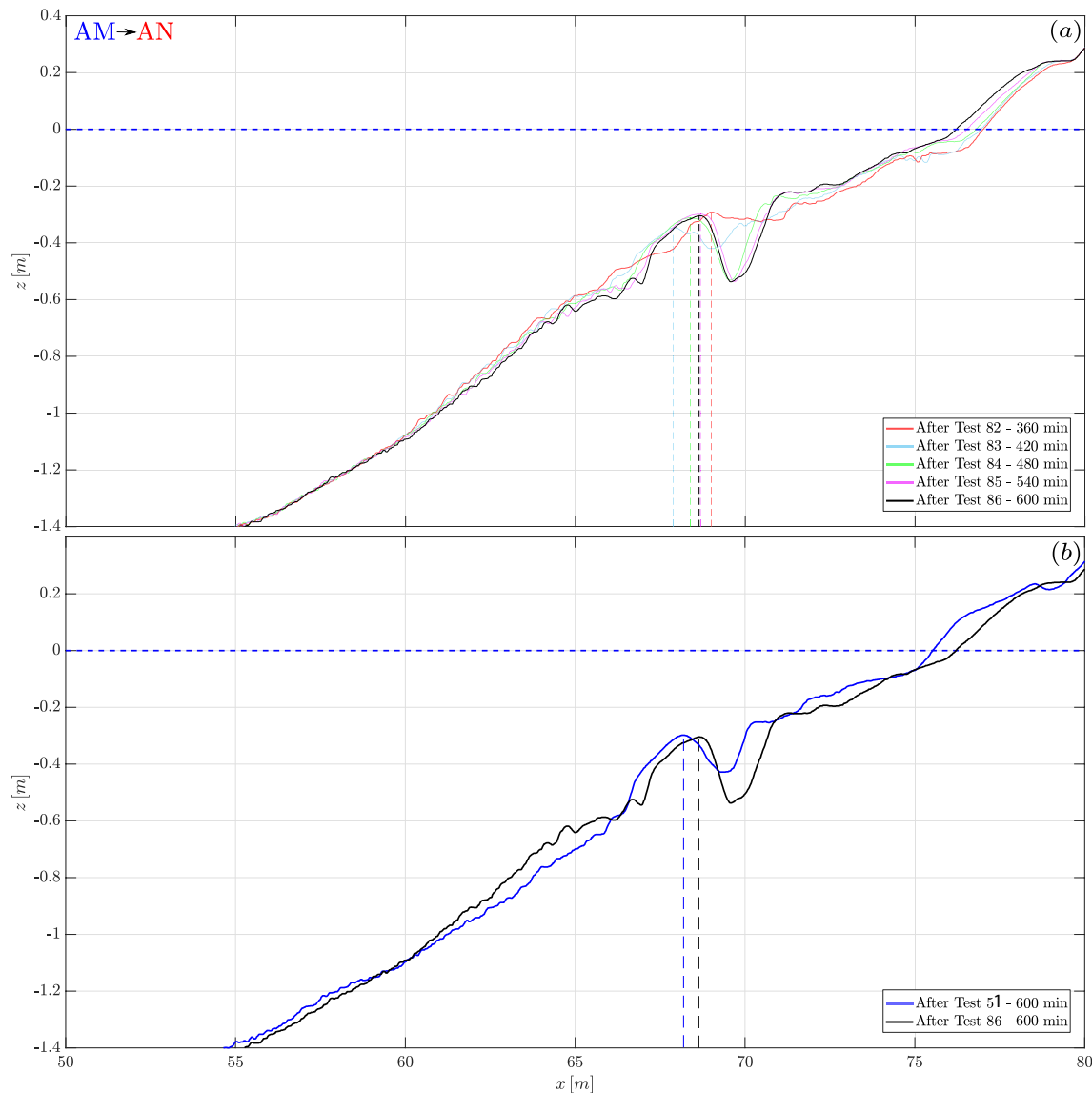


Figure 2. Example of accretive profile evolution after merging of the outer and inner bar (a). Still water level in dark blue dashed and profiles in various colors (solid lines). Final profiles at the end of sequences 1 and 2 (b). Bar maxima as dashed vertical lines.

slightly offshore while the new inner bar grows. Thus, whether commencing from E1 or E2 quasi-equilibrium profiles, after testing with wave condition A1 the final quasi-equilibrium profiles are relatively similar, characterized by outer bars at $x \approx 68$ m and inner bars at $x \approx 71$ m (Figure 2b). Note that the distance between bar and shoreline is almost the same after tests 51 and 86 and if the profiles are compared using a coordinate system with origin at the shoreline, both profiles are highly similar, especially onshore of the bar trough.

3.2. Hydrodynamics

3.2.1. Wave Heights and Breaking

Figure 3 indicates the ratio of wave height over water depth and wave breaking during AM (a) and AN (b). Data were ensemble-averaged for the tests considered representative of each morphological evolution (AM: 24, 25, 27, 30, 77, 79 and AN: 32, 34, 45, 47, 51, 65) and they are shown in cross-shore positions relative to the outer bar crest (x'), rather than absolute cross-shore positions (x). Short wave heights were calculated as described in Section 2.3 and a commonly-used depth-dependent breaking criterion (Miche, 1944) is used to show the breaking position in Figure 3.

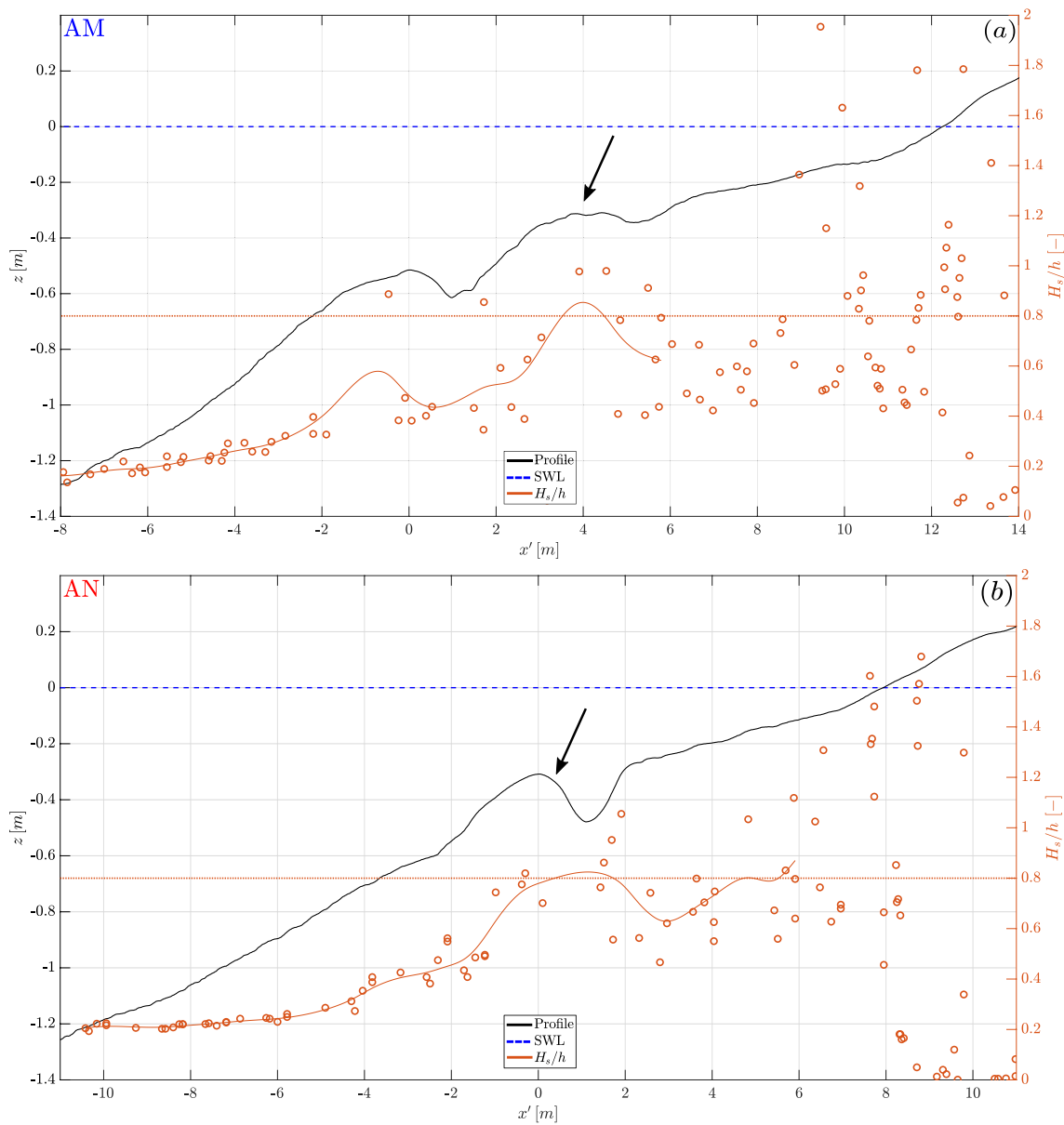


Figure 3. Significant short wave height over water depth and beach profiles ensemble-averaged over representative tests with merging outer bar (a) and non-merging outer bar (b) in cross-shore positions relative to outer bar crest. Still water level (blue dashed) and beach profiles (black) refer to left y-axis while orange scatter markers, reference lines (dotted) and smoothing-spline interpolated lines (solid) refer to right y-axis. Arrows indicate breakpoints.

During AM (AN) waves appear to break primarily on the inner (outer) bar (Figures 3a and 3b)—consistent with visual observations during the experiments. As the free-board over the outer bar crest is much larger during AM, this is not surprising. In fact, AM's free-board over the inner bar, rather than the outer, is similar to the free-board over the outer bar during AN. These differences originate from the antecedent erosive wave conditions: after E1 the outer bar was located farther offshore and featured a larger free-board than after E2 (Eichentopf, van der Zanden, et al., 2020). Note that water depth induces breaking via its influences on horizontal particle velocity and wave celerity (e.g., Peregrine, 1983).

3.2.2. Time-Averaged Velocities

Figure 4 shows the cross-shore evolution of time-averaged velocity measurements from the mobile frame during AM (a) and AN (b). Again, data are shown in x' -coordinates but this time focused on the outer bar

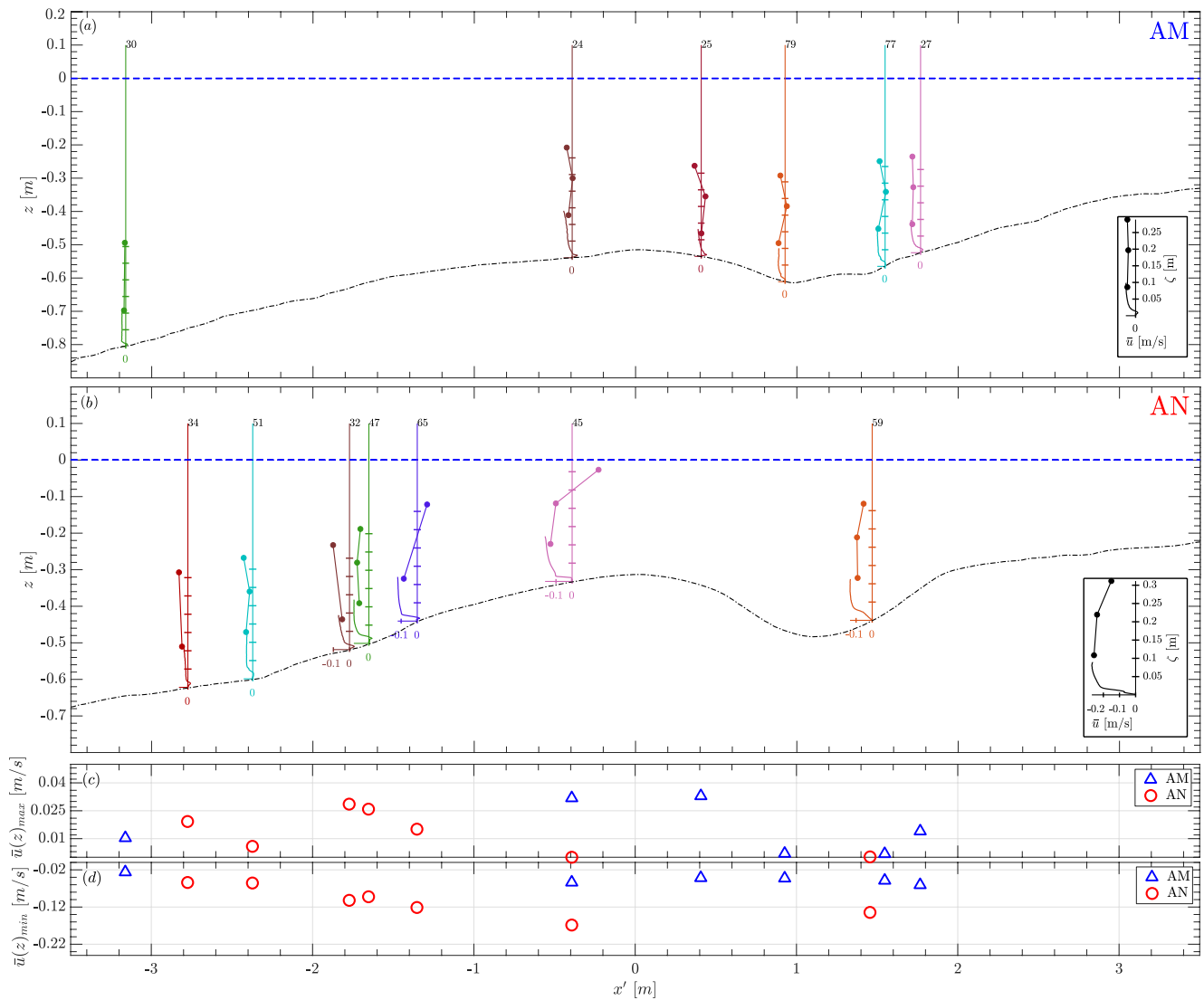


Figure 4. Time-averaged velocities in cross-shore positions relative to outer bar crest during merging (a) and non-merging (b) outer bar migration. Horizontal velocity profiles from Acoustic Concentration and Velocity Profiler (ACVP) (near-bed solid lines) and Acoustic Doppler Velocimeters (ADVs) (dots connected by solid lines) over ensemble-averaged beach profile (dashed-dotted black line) with still water level (dashed dark blue line); (c) Maximum time-averaged, depth-dependent onshore velocity measured by ACVP near the bed; (d) Maximum time-averaged, depth-dependent offshore velocity measured by ACVP and ADVs.

($-3.5 < x' < 3.5$ m). Good agreement between ACVP (solid lines) and ADV (dots connected by solid lines) measurements becomes visible.

In many tests there are time-averaged onshore velocities near the bed, probably caused by a dominance of progressive wave streaming over waveshape streaming (e.g., Kranenburg et al., 2012; Longuet-Higgins, 1953). When comparing AM to AN, maximum magnitudes are similar but their relative cross-shore locations are different (Figure 4c). During AM the maximum occurs slightly onshore of the outer bar crest (Figure 4c, triangles), with magnitudes decreasing in the bar trough but increasing again on the inner bar. During AN the maximum occurs on the offshore slope of the outer bar (Figure 4c, circles), with no time-averaged onshore velocities at the bar crest nor farther onshore.

Undertow (time-averaged offshore current) magnitudes over the outer bar are much lower under AM than AN (Figure 4c, compare triangles to circles). Whereas the maximum (negative) during AM occurs on the offshore slope of the inner bar ($x' = 1.8$ m), the maximum during AN occurs just offshore of the outer bar crest

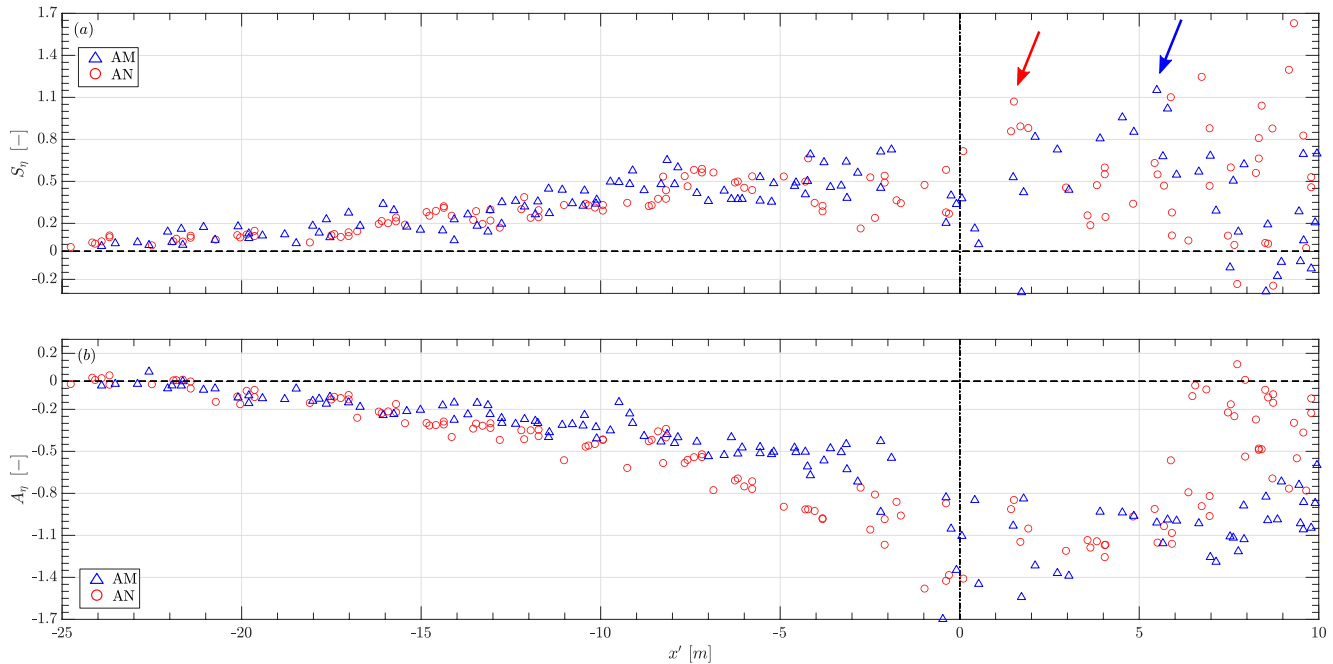


Figure 5. Water surface elevation skewness (a) and asymmetry (b) along the wave flume in cross-shore positions relative to outer bar crest. Dashed-dotted vertical lines indicate the position of outer bar crest and arrows indicate breakpoints.

($x' = -0.4$ m). There, AM features a local maximum but its magnitude is more than three times lower than under AN. Wave breaking is considered the most important forcing mechanism of undertow (e.g., Svendsen, 1984). Thus, the present results support the idea that during AM (AN) wave breaking is primarily associated with the inner (outer) bar (see Section 3.2.1). Most likely, even higher undertow magnitudes would have been measured during AM on top of the inner bar, but unfortunately no data are available.

3.2.3. Skewness and Asymmetry

Skewness and asymmetry characterize natural waves' deviation from the perfectly sinusoidal shape assumed in linear wave theory. High-pass filtered (as described in Section 2.3) water surface elevation measurements η_{sw} (omitting PT measurements close to the bar crest where waves get very nonlinear) were inserted in:

$$S_{\eta} = \frac{\overline{\eta_{sw}(t)^3}}{\sigma_{\eta_{sw}}^3} \quad (1)$$

to calculate skewness S_{η} , which represents the waves' asymmetry about the horizontal axis. The overbar in Equation 1 represents time-averaging and σ is the standard deviation. To calculate asymmetry A_{η} , which represents the waves' asymmetry about the vertical axis, η_{sw} in the previous equation was replaced with its Hilbert transform (Elgar, 1987). As a result, waves with pitched-forward shape have a negative A_{η} value.

In general, S_{η} and A_{η} show similar cross-shore evolution during AM and AN (Figure 5). However, S_{η} is observed to peak at $x' \approx 5$ m ($x' \approx 2$ m) during AM (AN), supporting (e.g., Babanin et al., 2007) the different breakpoint locations (see also Sections 3.2.1 and 3.2.2). Furthermore, A_{η} starts increasing farther offshore under AN - again consistent with an earlier breakpoint. In fact, the cross-shore evolution of S_{η} and A_{η} are closely related to water depth (which is lower in AN, see Figures 4a and 4b) and when plotting them over it (not shown for brevity), they are very similar—nearly independent of AM or AN. Note that the S_{η} and A_{η} cross-shore evolution shown (in reference to the outer bar crest) in Figure 5 originate from the same wave condition starting from different initial profiles.

3.2.4. Intrawave Hydrodynamics and Sediment Dynamics

Figure 6 presents ensemble-averaged measurements during AM at 1.8 m onshore of the outer bar crest (see Grossmann et al. (2022) for similar plots under E2, Grossmann et al. (2023) for a similar plot during AN). Three wave groups occur during T_r (delimited by vertical dashed lines in the figures) and short wave amplitudes are

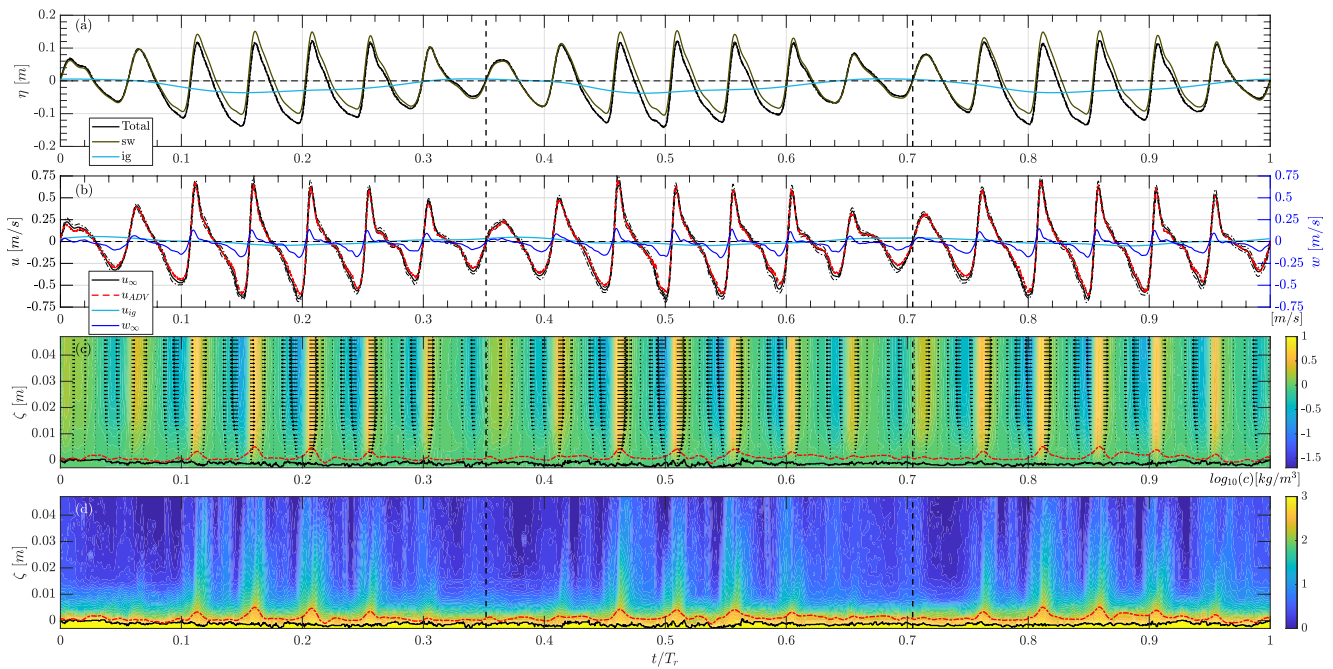


Figure 6. Hydrodynamic and sediment dynamics data in test 27 (AM) at 1.8 m onshore of the outer bar crest in the outer breaking zone. Vertical dashed lines indicate separation into wave groups. (a) Water surface elevations from PT shown before (black line with \pm one standard deviation as black dashed-dotted line) and after separation into short wave (dark green) and infragravity contributions (light blue); (b) Free stream velocities from Acoustic Concentration and Velocity Profiler (ACVP) (featuring \pm one standard deviation as black dashed-dotted line) and a co-located Acoustic Doppler Velocimeter, horizontal velocities referring to left y-axis and vertical velocity referring to right y-axis; (c) Near-bed velocity field from ACVP; (d) Near-bed concentration field from ACVP. Fields (c and d) referring to colorbars on their right and including instantaneous bed level (black) and upper limit of sheet flow layer (red dashed-dotted).

much larger than infragravity wave amplitudes. ADV measurements indicate good agreement with ACVP measurements of free-stream velocity taken at $\zeta = 0.05$ m (Figure 6b) and there is little deviation between the ensembles considered for ensemble-averaging.

The waves are visibly skewed and asymmetric but do not appear to have started breaking yet (Figures 6a and 6b). The u_∞ (measured at $\zeta = 0.05$ m) troughs (Figure 6b) are larger than farther offshore, indicating influence from offshore-directed undertow currents resulting from wave breaking farther onshore. Depth-dependent velocities, $u(z)$, are constant over $\zeta > 0.025$ m but show a “velocity overshoot” below (Figure 6c). This is typical for oscillatory boundary layer flows without wave breaking (e.g., Huang et al., 2010; van der A et al., 2011).

The main suspension events occur at phases of short wave crests (Figure 6d). The suspension plumes extend until $\zeta \approx 0.075$ m (not shown for brevity), there is a wider layer of large concentration near the bed and sediment is suspended for a longer fraction of T_r (than at $x' = 0.4$ m, see Figure S1d in Supporting Information S1). Nevertheless, the tendency of sediment to stay in suspension is still lower than during AN at $x' = -0.4$ m (test 45; see Figure 3d in Grossmann et al. (2023), presented as Figures S3d in Supporting Information S1). There, despite being located offshore of the outer bar crest, suspension plumes had larger vertical extents and sediment was continuously suspended for large shares of the time series. Furthermore, the waves were more asymmetric, consistent with Figure 5b, and velocity magnitudes were larger (compare Figure S3b in Supporting Information S1 to Figure 6b in the present publication).

3.3. Sediment Concentration and Transport

3.3.1. Linking Transport and Morphological Evolution

Figure 7 serves to connect the previously observed morphological evolution to net sediment transport rates during AM. As explained in Section 2.3, they can be calculated for each test over the entire active beach profile by inputting beach profile transect measurements into the Exner equation. Ensemble-averaging over all considered tests

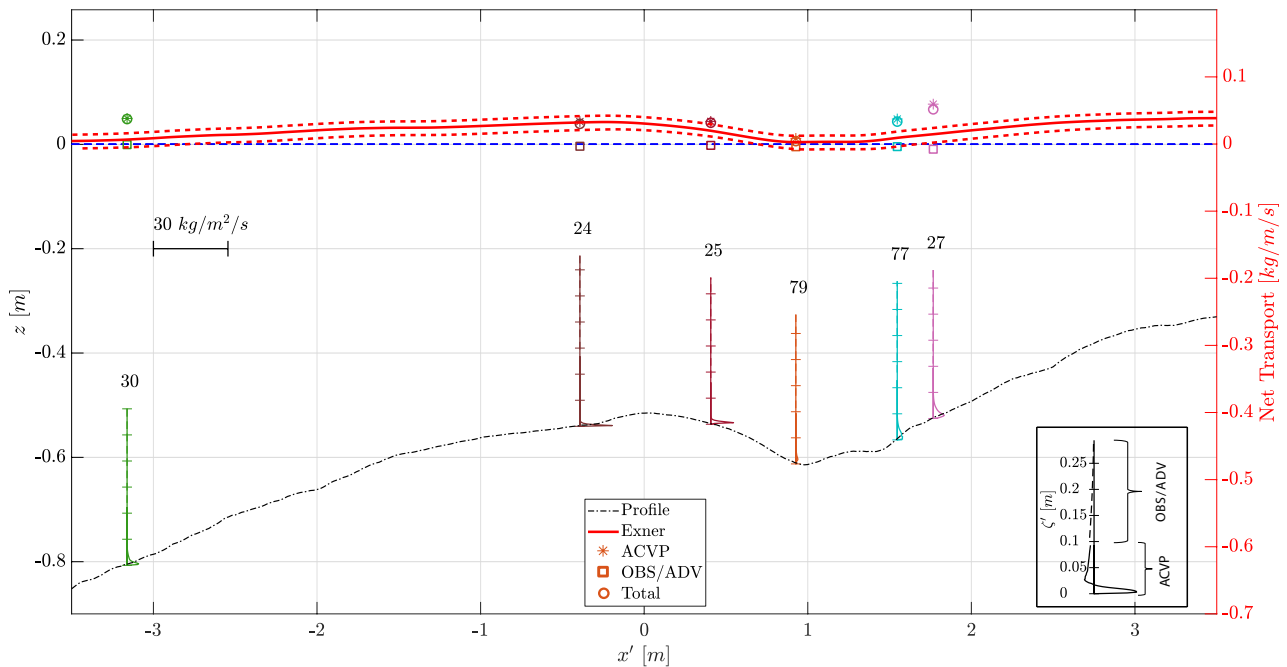


Figure 7. Net transport during accretive merging from the mechanical profiler, Acoustic Concentration and Velocity Profiler (ACVP) and Optical Backscatter Sensor (OBS)/Acoustic Doppler Velocimeter (ADV) in the vicinity of the outer bar crest. Profile transect measurements (red line referring to right y-axis) based on ensemble-averaging of Exner equation calculations in single tests with error bounds (red dashed lines) calculated as explained in accompanying text (Sections 2.3 and 3.3.1). ACVP and OBS/ADV measurements (stars and squares with color indicating respective tests) are based on depth-integration and time-averaging of instantaneous measurements of horizontal velocity and sediment concentration in the ζ' -coordinate system. They are shown separately and as their summation (circles). Additionally, depth-resolving net flux profiles from ACVP and OBS/ADV shown in their respective relative cross-shore positions with mini-axes according to sketch in the bottom right corner and scale as shown at $x' = -3$ m.

provides the red solid line shown in Figure 7. To quantify the influence of error accumulation in residuals and measurement inaccuracies, the same beach profile was measured three times in a row without sediment transport in between. Transport rates were then calculated and averaged over the available cross-shore extent and over the three measurements. The standard deviation amounted to 0.002 kg/m/s. Consequently, a conservative error bound of 0.01 kg/m/s was taken (red dashed lines shown in Figure 7). By depth-integrating and time-averaging ACVP and OBS/ADV instantaneous sediment flux measurements, total net transport rates (circle markers) at the cross-shore locations of the mobile frame can be obtained. When comparing them to the net transport from profile transect measurements, good agreement well within error bounds is observed.

During AM there is net onshore transport rate over the entire region surrounding the outer and inner bars (Figure 7 and cross-shore extent not shown for brevity). Cross-shore gradients in the transport rate result in a distinct pattern of morphological evolution over the outer bar: The increase of transport rate ($x' < -0.2$ m) results in erosion in the bar's offshore slope ($60 < x < 65$ m in Figure 1); the strong decrease of transport rate ($x' > 0.2$ m) results in accretion, filling the bar trough and contributing to outer bar dissipation and merging. During AN, where the outer bar maintained its shape, the gradient of net onshore transport rate decrease was much lower—matching the gradient of increase on the offshore side of the bar (see Figure 6 of Grossmann et al. (2023) presented as Figure S4 in Supporting Information S1).

3.3.2. Decomposed Net Sediment Fluxes

Resolving the vertical dimension of ACVP and OBS/ADV measurements (Figure 7; vertical profiles referring to mini-axes as shown in bottom right corner) provides additional details about the net transport. Note that, for brevity, only representative relative cross-shore locations are shown. Near the bed, the ACVP provided profiles of high vertical resolution. Certain tests feature shorter vertical extents because of larger morphological changes in the respective cross-shore location and because the ensemble with smallest vertical extent determined the vertical extent of the ensemble-average (as explained in detail in Grossmann et al. (2022)). The only considerable net flux is onshore-directed and occurs near the bed ($\zeta < 0.03$ m). Its magnitude follows a similar cross-shore evolution

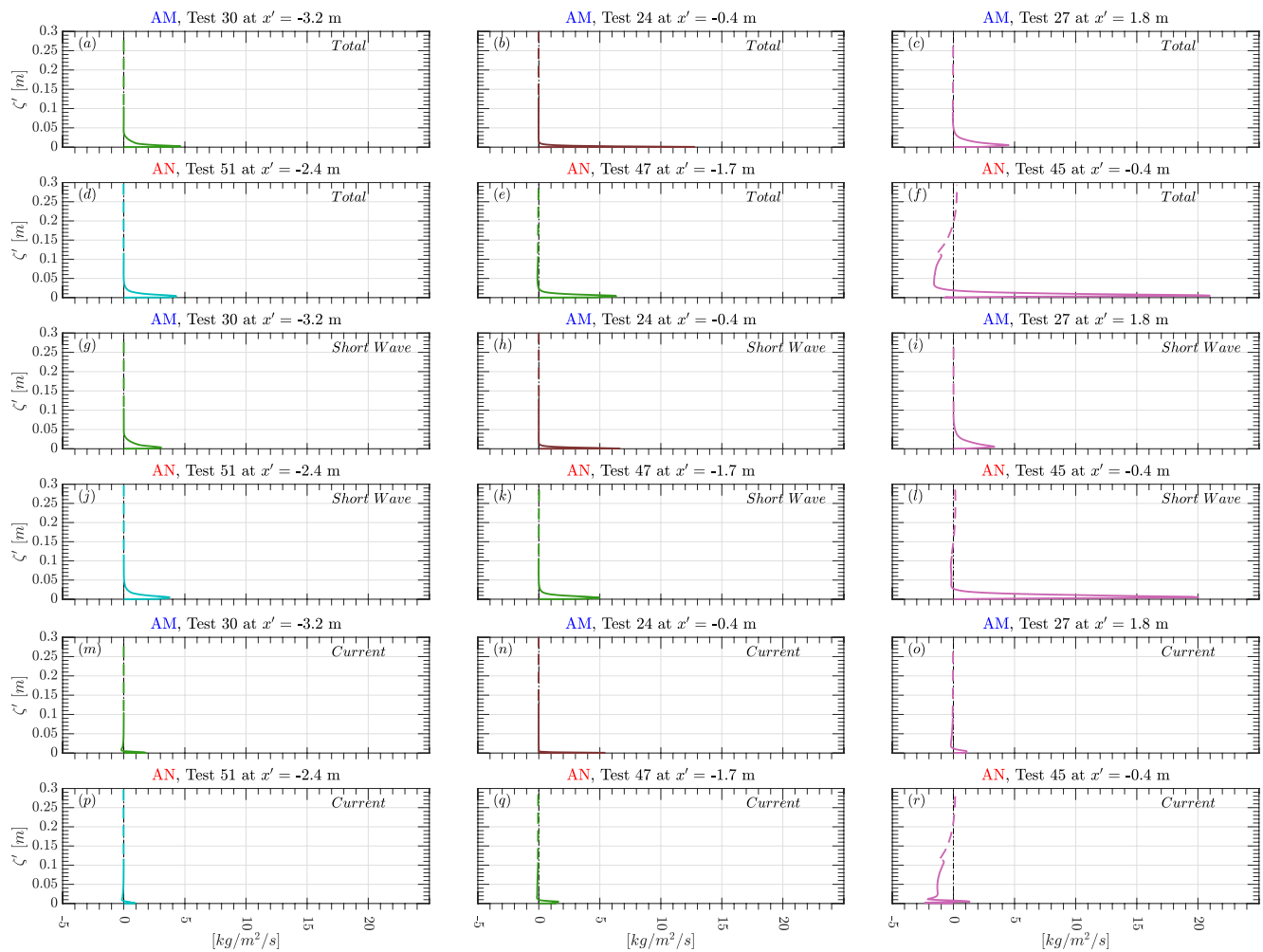


Figure 8. Representative decomposed net flux profiles during accretive merging (a, b, c, g, h, i, m, n, o) and accretive non-merging (d, e, f, j, k, l, p, q, r) in different cross-shore positions relative to outer bar crest. Panels on top of each other compare the two morphologies at different x' in total (a–f), short wave-related (g–l) and current-related (m–r) net flux.

as the total net transport rate from the Exner equation. Representative, relative cross-shore locations were chosen for comparing (decomposed) net sediment fluxes during AM and AN (Figure 8).

In contrast to AM, there is considerable suspended net offshore flux at $\zeta' > 0.025$ m during AN in locations close to the bar crest (Figures 8e and 8f). This results from offshore-directed currents (Figures 8q and 8r). Their influence becomes evident during AM close to the inner bar crest (Figure 8o), too, but to a lesser extent. The currents result from wave breaking and undertow, which occurred farther onshore under AM (see Sections 3.2.1–3.2.3). The near-bed net onshore fluxes visible during AM and AN (Figures 8a–8f) are related to the skewed and asymmetric short waves (Figures 8g–8l), which only feature considerable net flux contributions very close to the bed. Near-bed net onshore streaming also contributes to net onshore fluxes (e.g., Figures 8m, 8n, and 8p) but to a lesser extent. Interestingly, the interaction of offshore-directed undertow and onshore-directed streaming causes complicated current-related net flux profiles near the bed (Figures 8o, 8q, and 8r).

3.3.3. Depth-Integrated Transport Rates

Vertical profiles of net sediment fluxes are depth integrated over the whole domain available from the ACVP and OBS/ADV (as shown in Figure 7) to obtain (decomposed) net transport rates. During AM short wave-related transport rates are always onshore-directed (Figure 9a) and only increase on the offshore slope of the inner bar, consistent with the increased skewness and asymmetry shown in Figure 5. Current-related transport rates are

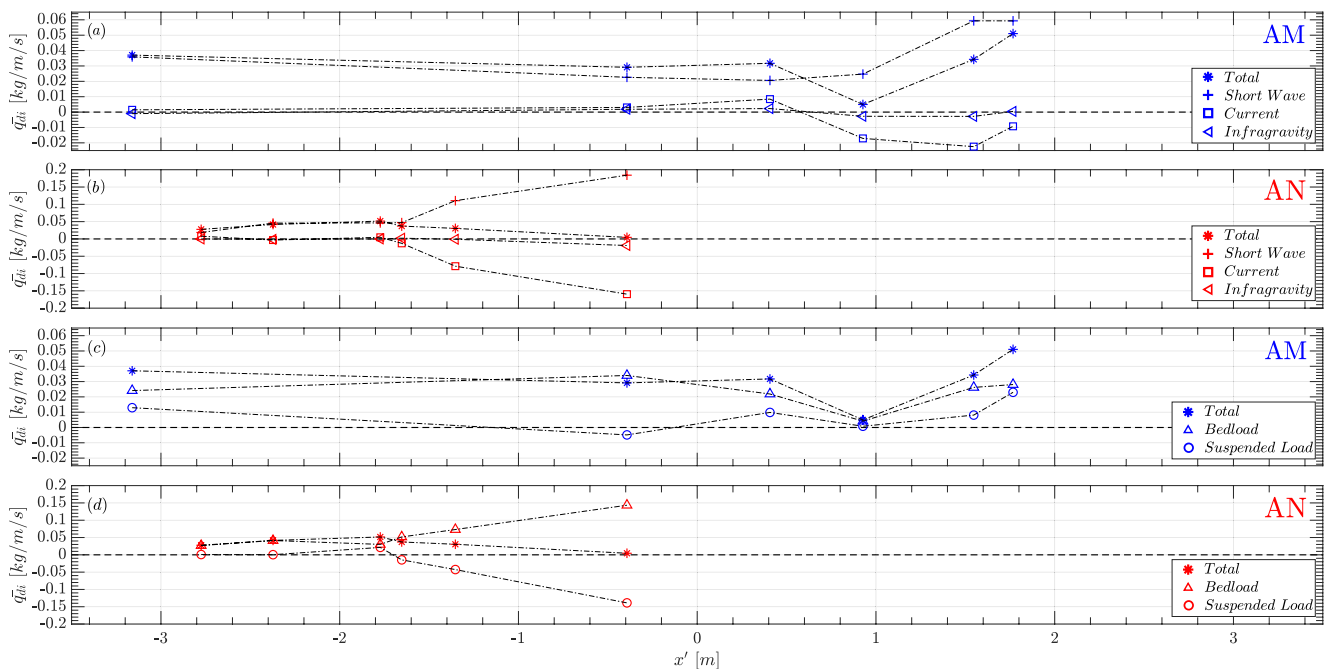


Figure 9. Depth-integrated (over entire vertical extent as shown in Figure 7a), time-averaged (net) sediment transport during accretive merging (a, c) and accretive non-merging (b, d) at cross-shore positions relative to the outer bar crest. (a, b) Frequency-decomposed ($0.117 \text{ Hz} < \text{short wave-related}$); (c, d) Vertically-decomposed. Note the changing y-axis limits.

onshore-directed up to the outer bar trough ($x' \leq 0.9 \text{ m}$), probably because of streaming in the wave boundary layer (Figure 4). Closer to the inner bar ($x' > 0.9 \text{ m}$) they become offshore-directed, which is consistent with the increased undertow and time-averaged concentration magnitudes (e.g., Figure 4 and concentration data not shown for brevity) and has a large influence on total net transport rate in the outer bar trough. In agreement with the tests during AN (Figure 9b), the infragravity-related transport is negligibly low compared to the other two components. Therefore, the balance between short wave-related onshore-directed and current-related (mainly) offshore-directed transport rate determines the total net transport rate.

During AN short wave-related net onshore transport already increased considerably on the outer bar offshore slope (in contrast to the inner bar offshore slope as observed during AM). Furthermore, much higher frequency-decomposed net transport rates were measured on the outer bar (e.g., up to one order of magnitude higher for the current-related transport rate). This is consistent with the differences in wave propagation and breaking (Section 3.2.1). As a result, the onset of suspended net offshore transport does not seem to have as large consequences on total net transport rate in the bar trough (Figure 6 in Grossmann et al. (2023) presented as Figure S4 in Supporting Information S1) as it did during AM (Figures 7 and 9), and the cross-shore gradient is much lower.

Sediment transport was also decomposed vertically on the basis of sheet flow layer elevations. Under both AM and AN, bedload follows a very similar cross-shore evolution as short-wave related net transport rate. The relation between suspended load and current-related transport rate is less clear under AM than AN. This might result from the very thin sheet flow layers under AM (e.g., Figure 6) so that a considerable share of short wave-related transport is accounted for as suspended transport.

4. Discussion

4.1. Initial Beach Profile Influence, Equilibrium and Bar Migration

The presented measurements have illustrated beach profile evolution under the same low energy wave condition (A1) but starting from different post-storm initial profiles. The final beach profile configurations after A1 are

relatively similar indicating a similar quasi-equilibrium situation controlled by the wave condition and characterized by an outer bar located at $x \approx 68$ m, an inner bar located at $x \approx 71$ m, and the shoreline located at $x \approx 76$ m. Although the final configuration is determined by the wave condition, the path to reach the final configuration is determined by the initial beach configuration showing bar dissipation and merging (AM), when the initial bar resulted from more energetic conditions, and onshore bar migration with bar maintenance, when the initial bar resulted from a less energetic storm (AN).

Similar behavior resulting from differences in the initial conditions has already been reported in laboratory experiments by Eichentopf et al. (2018) and Sánchez-Arcilla and Cáceres (2018) showing, similarly, bar dissipation or onshore bar migration depending on initial bar configuration. Furthermore, Eichentopf, Alsina, et al. (2020) showed a similar behavior in field experiments with relatively energetic wave conditions. They caused offshore or onshore bar migration depending on the initial bar being located landward or seaward of its position in the final configuration.

An equilibrium concept can be applied to evaluate the state of disequilibrium between beach profile and hydrodynamics, driving morphological evolution in equilibrium-type models (e.g., Birrien et al., 2018; Yates et al., 2009). Considering wave energy and dimensionless sediment fall velocities of antecedent hydrodynamics (Table 1), disequilibrium should have been larger at the start of AM than AN. In fact, there is a larger shoreline recession and a more reflective beach profile ($74 \leq x \leq 76$ m) at the start of AM (Figure 1). In terms of disequilibrium, AM should lead to larger and faster beach profile adjustments than AN. In this case AN can be interpreted as closer to the final equilibrium condition situation, resulting in onshore migration with bar maintenance, whereas AM is far from equilibrium, resulting in bar dissipation and merging. Nevertheless, behind the equilibrium explanation there are hydrodynamic and sediment transport processes that lead to such distinct behavior and they can be explained on the basis of the detailed measurements.

4.2. Sediment Transport Gradients and Wave Breaking

Cross-shore gradients in net transport rate cause morphological evolution. Around the outer bar, they are different between AM and AN (Section 3.3.1). During AN the cross-shore gradients on both sides of the bar are low and similar, so that it maintains its shape while migrating onshore. During AM the strong decrease in net onshore transport rate on the onshore side of the bar results in filling of the bar trough and merging with the inner bar. Note that the gradients are caused by the balance of onshore- and offshore-directed sediment transport processes. During AM, the balance between short wave-related net onshore and current-related net offshore transport shifts more rapidly (in terms of cross-shore extent) toward current-related transport than under AN.

This is a result of differences in wave breaking during AM and AN. During AN the waves break on the outer bar (see Section 3.2.1). Breaking is preceded by gradual increases in asymmetries (see Figure 5), in undertow (see Figure 4) and in sediment suspension (not shown for brevity). Less data is available onshore of the breakpoint but asymmetries gradually decrease (see Figure 5) and, most likely, undertow gradually decreases as well (e.g., van der Zanden et al., 2016). During AM, where waves only break (and asymmetries only increase) on the inner bar, the magnitude of frequency-decomposed transport rates on the outer bar (mainly short wave- and streaming-related net onshore) is much lower (Figures 9a and 9c, $-3 \leq x' \leq 0$ m). Thus, the onset of a low, current-related net offshore transport in the bar trough (Figure 9a, $x' = 0.95$ m, square marker and Figure S2n in Supporting Information S1) results in a considerable total net transport rate cross-shore gradient (Figure 9a, star markers). This current-related net offshore transport is probably caused by undertow resulting from wave breaking on the inner bar (continuity considerations).

Dissipation of the outer breaker bar during onshore migration under accretive conditions was observed in medium- (Baldock et al., 2017) and large-scale experiments (e.g., Eichentopf et al., 2018, SANDS and WISE 2; Eichentopf, van der Zanden, et al., 2020, A3). In this context, it was hypothesized that wave breaking and related sediment transport processes are crucial for maintaining the bar (e.g., Baldock et al., 2017; Mariño-Tapia et al., 2007; Wijnberg, 1996). Once the bar reaches a certain depth during offshore migration or a change to smaller wave heights shifts the depth-induced breakpoint farther onshore, the bar may become “inactive” (e.g., Birrien et al., 2018) - waves pass over it without breaking.

The present experiments confirm this hypothesis. When wave condition A1 was applied to E2 quasi-equilibrium profiles (leading to AN morphology—outer bar maintenance), the freeboard over the outer bar was small enough for waves to keep breaking close to it. The magnitude of asymmetry-related bedload net onshore-directed transport increased over the shoaling and breaker zones similarly as the suspended net offshore transport, balancing each other (Grossmann et al., 2022). As a result, cross-shore gradients in total net transport rate were low and similar on both sides of the bar. In E1 quasi-equilibrium profiles (AM morphology—outer bar dissipation) the outer bar was located farther offshore with larger freeboard and waves only broke on the inner bar (Section 3.2.1). As a result, the magnitude of asymmetry-related bedload net onshore-directed transport at the outer bar was much lower than during AN and there was very little current-related, suspended net offshore-directed transport. Consequently, the onset of larger undertow magnitude and larger sediment suspension, thus larger current-related net offshore transport, in the outer bar trough (from breaking further onshore, as explained previously), caused a large gradient in total net transport rate and filling of the bar trough. Simultaneously, the offshore slope of the outer bar eroded (Figure 1a, $61 < x < 65$ m), showing some similarity to the bar dissipation observed by Birrien et al. (2018) in their Figure 4a, $10 < x < 10.5$ m. However, in the present experiments the outer bar migrates rapidly and keeps its bar shape until attaching to the inner bar (merging).

4.3. Bar Migration and Beach Recovery

Outer bar migration is a characteristic feature of beach recovery. Nevertheless, other parts of the profile are important in beach recovery as well. Continuous shoreline recovery is observed during both AM and AN (Figure 1). But there are interesting differences just below SWL ($0.2 \leq d \leq 0.05$ m). While AM shows continuous accretion, 120 min of testing pass before accretion starts under AN. This might be linked to the inner bar position and wave breaking. During AM the inner bar (which will later become the new outer bar) does not change in position, maintaining its freeboard and only steepening its offshore slope. This indicates its role as a sediment source for the accretion just onshore of it. During AN, on the other hand, the shape of the inner bar is not as accentuated so that it might be less effective as a sediment source. Only as the outer bar reaches a similar position and freeboard as the inner bar during AM ($x \approx 68.5$ m and ≈ 0.3 m), does similar accretion just below SWL start (Figure 1b, After Test 45). Furthermore, in the present water depths AM is characterized by slightly larger wave height over water depth (Figure 3), asymmetry and skewness (not shown for brevity) than AN, potentially leading to increased net onshore transport and accretion. This indicates the importance of bar position, and the related wave propagation, for morphological evolution even onshore of the bars.

Field studies observed that the proximity of the bar to the shoreline was important for the shoreline recovery rate (e.g., Phillips et al., 2017) and the success of beach recovery (e.g., Ruiz de Alegría-Arzaburu & Vidal-Ruiz, 2018). In this context, the present study highlights the importance of transition to a different type of accretive morphology (AM to AN) after bar merging (Figure 1a followed by Figure 2a). As a result, the shoreline recovers much more rapidly for the remaining 240 min of testing after the merging at the end of AM (Figure 2a).

5. Conclusions

Sediment transport processes in the shoaling and outer breaking zone under an accretive wave condition ($\Omega = 1.44$) were investigated through large-scale laboratory experiments. Starting from different initial, post-storm beach profiles, the outer bar was observed to merge with the inner and dissipate (AM morphology) or maintain its form (AN morphology) during onshore migration. Based on the results we conclude the following:

1. In spite of different initial profiles, application of wave condition A1 for a sufficient amount of time led to relatively similar quasi-equilibrium beach profiles. However, the morphological evolution toward quasi-equilibrium was different (AM and AN).
2. In contrast to AN, waves during AM passed the outer bar and only broke on the inner bar. As both AM and AN featured the same wave condition, this resulted from their differing initial beach profiles. Before AM, erosive condition E1 had produced an outer bar farther offshore (≈ 2 m) and with larger freeboard (≈ 0.15 m) than the outer bar before AN (which was produced by the less-energetic erosive condition E2).
3. As a result, transport processes around the outer bar were different during AM and AN. The former mainly featured bedload transport related to short wave asymmetries while the latter included suspended transport linked to wave breaking. During AM, such suspended transport only became visible onshore of the outer bar trough.

4. The differences in morphological evolution were related to cross-shore gradients in sediment transport rate. In contrast to AN, AM featured a strong decrease of net onshore transport rate in the outer bar's trough, leading to bar merging. This gradient was caused by the onset of a relatively high (compared to onshore-directed components) suspended net offshore transport (resulting from undertow and time-averaged sediment suspension) induced by wave breaking over the inner bar.
5. Morphological evolution of the outer bar and the shoreline were linked. AM was mainly associated with rapid accretion just below SWL ($0.2 \leq d \leq 0.05$ m). In AN, which sometimes followed bar merging at the end of AM, shoreline recovery ($d \geq 0$ m) was more evident.

Because of their high detail, the data presented in this article may be of particular interest for the further development of sediment transport and morphological models. They are freely available online (see Data Availability Statement).

Data Availability Statement

For data related to this article, visit <https://doi.org/10.5281/zenodo.7085619>.

Acknowledgments

We thank Dr. Tom Baldock and Dr. Marissa Yates for their valuable comments which helped to improve the manuscript. The experiments described in this work were funded by the European Community's Horizon 2020 Programme through the grant to the budget of the Integrated Infrastructure Initiative HYDRALAB+, Contract no. 654110, and were conducted as part of the transnational access project RESIST. FG acknowledges funding from the Agency for Management of University and Research Grants (AGAUR). DH acknowledges funding from the French DGA funded ANR ASTRID Maturation project MESURE (ANR-16-ASMA-0005-01). JA acknowledges funding from the Serra Hünter Programme (SHP). We wish to thank fellow RESIST researchers and the CIEM staff (Joaquim Sospedra, Oscar Galego, Dr. Andrea Marzeddu and Dr. Iván Cáceres) for their contributions to the experiments.

References

- Babanin, A., Chalikov, D., Young, I., & Savelyev, I. (2007). Predicting the breaking onset of surface water waves. *Geophysical Research Letters*, *34*(7), L07605. <https://doi.org/10.1029/2006GL029135>
- Baldock, T. E., Alsina, J. M., Cáceres, I., Vicinanza, D., Contestabile, P., Power, H., & Sánchez-Arcilla, A. (2011). Large-scale experiments on beach profile evolution and surf and swash zone sediment transport induced by long waves, wave groups and random waves. *Coastal Engineering*, *58*(2), 214–227. <https://doi.org/10.1016/j.coastaleng.2010.10.006>
- Baldock, T. E., Birrien, F., Atkinson, A., Shimamoto, T., Wu, S., Callaghan, D. P., & Nielsen, P. (2017). Morphological hysteresis in the evolution of beach profiles under sequences of wave climates—Part 1; observations. *Coastal Engineering*, *128*, 92–105. <https://doi.org/10.1016/j.coastaleng.2017.08.005>
- Birrien, F., Atkinson, A., Shimamoto, T., & Baldock, T. E. (2018). Hysteresis in the evolution of beach profile parameters under sequences of wave climates—Part 2; Modelling. *Coastal Engineering*, *133*, 13–25. <https://doi.org/10.1016/j.coastaleng.2017.12.001>
- Bonneton, P., Lannes, D., Martins, K., & Michallet, H. (2018). A nonlinear weakly dispersive method for recovering the elevation of irrotational surface waves from pressure measurements. *Coastal Engineering*, *138*, 1–8. <https://doi.org/10.1016/j.coastaleng.2018.04.005>
- Cheng, J., & Wang, P. (2018). Dynamic equilibrium of sandbar position and height along a low wave energy micro-tidal coast. *Continental Shelf Research*, *165*, 120–136. <https://doi.org/10.1016/j.csr.2018.05.004>
- Davidson, M. A., Splinter, K. D., & Turner, I. L. (2013). A simple equilibrium model for predicting shoreline change. *Coastal Engineering*, *73*, 191–202. <https://doi.org/10.1016/j.coastaleng.2012.11.002>
- Dean, R. G. (1977). Equilibrium beach profiles: U.S. Atlantic and Gulf coasts. Ocean engineering report no. 12.
- Dohmen-Janssen, C. M., Hassan, W. N., & Ribberink, J. S. (2001). Mobile-bed effects in oscillatory sheet flow. *Journal of Geophysical Research*, *106*(C11), 27103–27115. <https://doi.org/10.1029/2000JC000513>
- Dubarbier, B., Castelle, B., Mariéu, V., & Ruessink, B. G. (2015). Process-based modeling of cross-shore sandbar behavior. *Coastal Engineering*, *95*, 35–50. <https://doi.org/10.1016/j.coastaleng.2014.09.004>
- Eichentopf, S., Alsina, J. M., Christou, M., Kuriyama, Y., & Karunaratna, H. (2020). Storm sequencing and beach profile variability at Hasaki, Japan. *Marine Geology*, *424*, 106153. <https://doi.org/10.1016/j.margeo.2020.106153>
- Eichentopf, S., Cáceres, I., & Alsina, J. M. (2018). Breaker bar morphodynamics under erosive and accretive wave conditions in large-scale experiments. *Coastal Engineering*, *138*, 36–48. <https://doi.org/10.1016/j.coastaleng.2018.04.010>
- Eichentopf, S., van der Zanden, J., Cáceres, I., Baldock, T. E., & Alsina, J. M. (2020). Influence of storm sequencing on breaker bar and shoreline evolution in large-scale experiments. *Coastal Engineering*, *157*, 103659. <https://doi.org/10.1016/j.coastaleng.2020.103659>
- Elgar, S. (1987). Relationships involving third moments and bispectra of a harmonic process. *IEEE Transactions on Acoustics, Speech, & Signal Processing*, *35*(12), 1725–1726. <https://doi.org/10.1109/TASSP.1987.1165090>
- Fromant, G., Mieras, R. S., Revil-Baudard, T., Puleo, J. A., Hurther, D., & Chauchat, J. (2018). On bedload and suspended load measurement performances in sheet flows using acoustic and conductivity profilers. *Journal of Geophysical Research: Earth Surface*, *123*(10), 2546–2562. <https://doi.org/10.1029/2018JC014406>
- Gallagher, E. L., Elgar, S., & Guza, R. T. (1998). Observations of sand bar evolution on a natural beach. *Journal of Geophysical Research*, *103*(C2), 3203–3215. <https://doi.org/10.1029/97JC02765>
- Grossmann, F. G., Hurther, D., van der Zanden, J., Cáceres, I., Sánchez-Arcilla, A., & Alsina, J. M. (2022). Near-bed sediment transport during offshore bar migration in large-scale experiments. *Journal of Geophysical Research: Oceans*, *127*, e2021JC017756. <https://doi.org/10.1029/2021JC017756>
- Grossmann, F. G., Hurther, D., van der Zanden, J., Sánchez-Arcilla, A., & Alsina, J. M. (2023). Near-bed sediment transport processes during onshore bar migration in large-scale experiments: Comparison with offshore bar migration. *Journal of Geophysical Research: Oceans*, *128*(3), e2022JC018998. <https://doi.org/10.1029/2022JC018998>
- Hoefel, F., & Elgar, S. (2003). Wave-induced sediment transport and sandbar migration. *Science*, *299*(5614), 1885–1887. <https://doi.org/10.1126/science.1081448>
- Huang, Z.-C., Hwung, H.-H., Hsiao, S.-C., & Chang, K.-A. (2010). Laboratory observation of boundary layer flow under spilling breakers in surf zone using particle image velocimetry. *Coastal Engineering*, *57*(3), 343–357. <https://doi.org/10.1016/j.coastaleng.2009.11.004>
- Hurther, D., Thorne, P. D., Bricault, M., Lemmin, U., & Barnoud, J.-M. (2011). A multi-frequency Acoustic Concentration and Velocity Profiler (ACVP) for boundary layer measurements of fine-scale flow and sediment transport processes. *Coastal Engineering*, *58*(7), 594–605. <https://doi.org/10.1016/j.coastaleng.2011.01.006>

- Kranenburg, W. M., Ribberink, J. S., Uittenbogaard, R. E., & Hulscher, S. J. M. H. (2012). Net currents in the wave bottom boundary layer: On waveshape streaming and progressive wave streaming. *Journal of Geophysical Research*, *117*, F3. <https://doi.org/10.1029/2011JF002070>
- Kuriyama, Y. (2002). Medium-term bar behavior and associated sediment transport at Hasaki, Japan. *Journal of Geophysical Research*, *107*(C9), 3132. <https://doi.org/10.1029/2001JC000899>
- Longuet-Higgins, M. S. (1953). Mass transport in water waves. *Philosophical Transactions of the Royal Society of London Series A: Mathematical and Physical Sciences*, *245*(903), 535–581. <https://doi.org/10.1098/rsta.1953.0006>
- Mariño-Tapia, I. J., Russel, P. E., O'Hare, T. J., Davidson, M. A., & Huntley, D. A. (2007). Cross-shore sediment transport on natural beaches and its relation to sandbar migration patterns: I. Field observations and derivation of a transport parameterization. *Journal of Geophysical Research*, *112*(C3), C03001. <https://doi.org/10.1029/2005JC002893>
- Miche, R. (1944). *Mouvements ondulatoires de la mer en profondeur constante ou décroissante*. Annales des Ponts et Chaussées.
- Mieras, R. S., Puleo, J. A., Anderson, D., Hsu, T.-J., Cox, D. T., & Calantoni, J. (2019). Relative contributions of bed load and suspended load to sediment transport under skewed-asymmetric waves on a sandbar crest. *Journal of Geophysical Research: Oceans*, *124*(2), 1294–1321. <https://doi.org/10.1029/2018JC014564>
- Peregrine, D. H. (1983). Breaking waves on beaches. *Annual Review of Fluid Mechanics*, *15*(1), 149–178. <https://doi.org/10.1146/annurev.fl.15.010183.001053>
- Phillips, M. S., Harley, M. D., Turner, I. L., Splinter, K. D., & Cox, R. J. (2017). Shoreline recovery on wave-dominated sandy coastlines: The role of sandbar morphodynamics and nearshore wave parameters. *Marine Geology*, *385*, 146–159. <https://doi.org/10.1016/j.margeo.2017.01.005>
- Rafati, Y., Hsu, T. J., Elgar, S., Raubenheimer, B., Quataert, E., & van Dongeren, A. (2021). Modeling the hydrodynamics and morphodynamics of sandbar migration events. *Coastal Engineering*, *166*, 103885. <https://doi.org/10.1016/j.coastaleng.2021.103885>
- Ruiz de Alegría-Arzaburu, A., & Vidal-Ruiz, J. (2018). Beach recovery capabilities after El Niño 2015–2016 at Ensenada beach, Northern Baja California. *Ocean Dynamics*, *68*(6), 749–759. <https://doi.org/10.1007/s10236-018-1164-6>
- Sánchez-Arcilla, A., & Cáceres, I. (2018). An analysis of nearshore profile and bar development under large scale erosive and accretive waves. *Journal of Hydraulic Research*, *56*(2), 231–244. <https://doi.org/10.1080/00221686.2017.1315748>
- Sánchez-Arcilla, A., Cáceres, I., van Rijn, L. C., & Grüne, J. (2011). Revisiting mobile bed tests for beach profile dynamics. *Coastal Engineering*, *58*(7), 583–593. <https://doi.org/10.1016/j.coastaleng.2011.01.005>
- Sánchez-Arcilla, A., Roelvink, J. A., O'Connor, B. A., Reniers, A., & Jimenez, J. A. (1994). The Delta Flume '93 experiment. *Coastal Dynamics*, *94*, 488–502.
- Svendsen, I. A. (1984). Mass flux and undertow in a surf zone. *Coastal Engineering*, *8*(4), 347–365. [https://doi.org/10.1016/0378-3839\(84\)90030-9](https://doi.org/10.1016/0378-3839(84)90030-9)
- Trowbridge, J., & Young, D. (1989). Sand transport by unbroken water waves under sheet flow conditions. *Journal of Geophysical Research*, *94*(C8), 10971–10991. <https://doi.org/10.1029/JC094iC08p10971>
- van der A, D. A., O'Donoghue, T., Davies, A., & Ribberink, J. S. (2011). Experimental study of the turbulent boundary layer in acceleration-skewed oscillatory flow. *Journal of Fluid Mechanics*, *684*, 251–283. <https://doi.org/10.1017/jfm.2011.300>
- van der Zanden, J., Van Der, A. D. A., Hurther, D., Cáceres, I., O'Donoghue, T., & Ribberink, J. S. (2016). Near-bed hydrodynamics and turbulence below a large-scale plunging breaking wave over a mobile barred bed profile. *Journal of Geophysical Research: Oceans*, *121*(8), 6482–6506. <https://doi.org/10.1002/2016JC011909>
- van Rijn, L. C., Tonnon, P. K., & Walstra, D. J. R. (2011). Numerical modelling of erosion and accretion of plane sloping beaches at different scales. *Coastal Engineering*, *58*(7), 637–655. <https://doi.org/10.1016/j.coastaleng.2011.01.009>
- Wijnberg, K. M. (1996). On the systematic decay of offshore breaker bars. *Coastal Engineering Proceedings*, *1*(25). <https://icce-ojs-tamu.tdl.org/icce/index.php/icce/article/view/5493>
- Wright, L. D., & Short, A. C. (1984). Morphodynamic variability of surf zones and beaches: A synthesis. *Marine Geology*, *56*(1–4), 93–118. [https://doi.org/10.1016/0025-3227\(84\)90008-2](https://doi.org/10.1016/0025-3227(84)90008-2)
- Yates, M. L., Guza, R. T., & O'Reilly, W. C. (2009). Equilibrium shoreline response: Observations and modeling. *Journal of Geophysical Research*, *114*(C9), C09014. <https://doi.org/10.1029/2009JC005359>
- Yoon, H., & Cox, D. (2010). Large-scale laboratory observations of wave breaking turbulence over an evolving beach. *Journal of Geophysical Research*, *115*(C10), C10007. <https://doi.org/10.1029/2009JC005748>